Thickness dependence of spin Hall angle of Au grown on Y_{3}Fe_{5}O_{12} epitaxial films

Jack T. Brangham, Keng-Yuan Meng, Angela S. Yang, James C. Gallagher, Bryan D. Esser, Shane P. White, Sisheng Yu, David W. McComb, P. Chris Hammel, and Fengyuan Yang

Phys. Rev. B **94**, 054418 — Published 16 August 2016

DOI: 10.1103/PhysRevB.94.054418

Thickness Dependence of Spin Hall Angle of Au Grown on $Y_3Fe_5O_{12}$ Epitaxial Films

Jack T. Brangham[1], Keng-Yuan Meng[1], Angela S. Yang[1], James C. Gallagher[1], Bryan D. Esser[2], Shane P. White[1], Sisheng Yu[1], David W. McComb[2], P. Chris Hammel[1], and Fengyuan Yang[1]

[1]Department of Physics, The Ohio State University, Columbus, OH, 43210, USA

[2]Center for Electron Microscopy and Analysis, Department of Materials Science and Engineering, The Ohio State University, Columbus, OH, 43212, USA

Abstract

We measure the spin Hall angle in Au layers of 5 to 100 nm thicknesses by spin pumping from $Y_3Fe_5O_{12}$ epitaxial films grown by ultrahigh vacuum, off-axis sputtering. We observe a striking increase in the spin Hall angle for Au layers thinner than the measured spin diffusion length of 12.6 nm. In particular, the 5 nm Au layer shows a large spin Hall angle of 0.087, compared to those of 0.016 and 0.017 for the 50 and 100 nm Au layers, respectively, suggesting that the top surface plays a dominant role in spin Hall physics when the spin current is able to reach it. Other spin pumping related parameters, including Gilbert damping enhancement, interfacial spin mixing conductance, and spin current are also determined for Au layers of various thicknesses. Given the pervasive role ultrathin films in electrical and spin transport applications, this result emphasizes the importance of considering the impact of the top surface and reveals the possibility of tuning critical spin parameters by film thickness.

PACS: 72.25.Ba, 76.50.+g, 72.25.Mk, 75.70.Ak

The spin Hall effect (SHE) and its reciprocal process, the inverse spin Hall effect (ISHE), have generated intense interest in recent years as a means of producing, manipulating, and detecting spin currents in nonmagnetic materials, opening new routes to spin-based electronic applications.[1-13] The ability to convert an unpolarized electrical current into a spin current can be quantitatively described by the spin Hall angle (θ_{SH}).[14,15] θ_{SH} is a material-specific quantity that arises from spin-orbit coupling (SOC). Its magnitude and sign are primarily determined by atomic number, and for transition metals, by the *d*-orbital filling.[16-19] Au is a transition metal with a large atomic number of 79, which should lead to strong SOC and hence a large θ_{SH}. As a result, both SHE and ISHE in Au have been extensively studied by various techniques.[20-28] These studies have reported values of θ_{SH} for Au between 0.25% (0.0025) and 11% (0.11). This broad range of measured values can be attributed to the use of varying experimental techniques and to Au layer thicknesses. Previously, we have studied ISHE in a number of transition metals using $Y_3Fe_5O_{12}$ (YIG) based ferromagnetic resonance (FMR) spin pumping, which provides very large ISHE signals.[18] In this article, we report systematic measurements of the spin Hall angle for a series of Au films of thicknesses between 5 and 100 nm by spin pumping in YIG/Au bilayers.

The YIG(16 nm) films are epitaxially grown on (111)-oriented $Gd_3Ga_5O_{12}$ (GGG) substrates by ultrahigh vacuum, off-axis sputtering.[29-31] The substrate temperature is 750°C during film growth and the substrate rotates at 10 degrees/sec to achieve optimal film uniformity. A radio-frequency power of 60 W is used for YIG sputtering, which gives a deposition rate of 0.51 nm/min. The Au is grown *in-situ* on the YIG film at room temperature by off-axis DC sputtering at a deposition rate of 2.24 nm/min. The crystalline quality of the YIG films and YIG/Au bilayers are examined by X-ray diffraction (XRD) and X-ray reflectivity (XRR) using a

Bruker D8 Discover high-resolution triple-axis X-ray diffractometer, and scanning transmission electron microscopy (STEM) using an FEI probe-corrected Titan^3 80-300 S/TEM.

Figure 1(a) shows a 2θ-ω XRD scan of a 16 nm YIG on GGG(111), which exhibits clear Laue oscillations. Despite the shadowing of the YIG(444) peak by the GGG(444), we can identify the location of YIG(444) from the Laue oscillations. We obtain an out-of-plane lattice constant of 12.431 Å for the YIG film, which is slightly larger than the bulk value of 12.376 Å. Figure 1(b) shows an XRR spectrum for a YIG(16 nm)/Au(41 nm) bilayer together with a simulation by Bruker LEPTOS software. The simulation gives the thicknesses of the YIG(16 nm) and Au(41 nm) layers as well as a YIG/Au interfacial roughness of less than 1 Å. Figure 1(c) shows a high angle annular dark field (HAADF) STEM image of the YIG/GGG(111) interface viewed along the <110> direction, revealing the clear garnet ordering in both the YIG film and the GGG substrate as well as complete epitaxy between them. No structural defects were detected in all areas examined by STEM. The XRD and STEM results demonstrate that the YIG films have very high crystalline quality and a clean, sharp interface with Au.

Figure 2(a) schematically shows the experimental setup for FMR spin pumping and ISHE detection of the spin current in a series of YIG(16 nm)/Au(t_{Au}) bilayers, where t_{Au} is the Au thickness and all samples are approximately 1 mm × 5 mm. A DC magnetic field (H) is applied in the film plane and perpendicular to the sample length, while an ISHE voltage is measured across the length of the Au layer. Spin pumping measurements are performed in a Bruker electron paramagnetic resonance (EPR) spectrometer with a microwave cavity at a radio frequency (rf) of f = 9.65 GHz and a microwave power of P_{rf} = 200 mW. While a DC in-plane magnetic field is swept across the YIG resonant field (H_{res}), the rf field is applied to excite the uniform precession of the YIG magnetization. At the Au interface, this excited precession

transfers angular momentum to the conduction electrons in Au, generating a pure spin current, $\boldsymbol{J_s}$, in the Au. The spin current travels through the Au perpendicular to the plane, and is converted into a transverse charge current, $\boldsymbol{J_c}$, due to ISHE. This results in a voltage difference, V_{ISHE}, between the two ends of the Au layer, measured by a Keithley 2182A Nanovoltmeter.

Figure 2(b) shows three representative V_{ISHE} vs $H - H_{\mathrm{res}}$ plots for YIG/Au bilayers with Au layer thicknesses of 5, 30, 50, and 100 nm. The ISHE voltage is as high as 143 μV for the 5 nm Au sample and decreases for thicker Au. The magnitude of V_{ISHE} depends on a number of parameters given by,[5,6,14,32]

$$V_{\mathrm{ISHE}} = \frac{-e\theta_{\mathrm{SH}}}{\sigma_{\mathrm{Au}} t_{\mathrm{Au}}} \lambda_{\mathrm{SD}} \tanh\left(\frac{t_{\mathrm{Au}}}{2\lambda_{\mathrm{SD}}}\right) g_{\uparrow\downarrow} f L P \left(\frac{\gamma h_{\mathrm{rf}}}{4\pi f \alpha}\right)^2, \quad (1)$$

where e is the electron charge, σ_{Au} is the Au conductivity, λ_{SD} is the spin diffusion length in Au, $g_{\uparrow\downarrow}$ is the effective interfacial spin mixing conductance, L is the sample length, $P = 1.21$ is a factor due to the ellipticity of magnetization precession,[5] γ is the gyromagnetic ratio, $h_{\mathrm{rf}} = 0.25$ Oe is the rf magnetic field in the EPR cavity at $P_{\mathrm{rf}} = 200$ mW, and α is the Gilbert damping constant of YIG. Figure 2(c) shows the derivative spectra of FMR absorption for a bare YIG(16 nm) film and three YIG(16 nm)/Au bilayers with 5, 30, and 50 nm Au layers. The FMR linewidth increases from $\Delta H = 4.3$ Oe for the bare YIG to 7.5, 19, and 20 Oe for the 5, 30, and 50 nm Au on YIG, respectively. This broadening of the linewidth indicates a clear damping enhancement and its dependence on the Au thickness.

To calculate θ_{SH}, we focus on our measurements of λ_{SD} and $g_{\uparrow\downarrow}$, as the measurements of the other parameters are straightforward. The spin diffusion length of the Au layers is determined by the dependence of spin current on Au thickness. Figure 3(a) shows the ISHE voltages of different Au thicknesses from 5 to 100 nm. Since V_{ISHE} depends on the resistivity/conductivity of the Au layers, we plot ρ vs t_{Au} in Fig. 3(b). The resistivity of the 5 nm

Au film is about 2 to 3 times higher than the other Au films due to the dominance of surface scattering for very thin films. Figure 3(c) shows V_{ISHE}/Rw, where R and w are the resistance and sample width, respectively, of each YIG/Au bilayer. V_{ISHE}/Rw is the ISHE-induced transverse charge current normalized by sample width, which is proportional to the spin current pumped into the Au layers. Assuming λ_{SD} is constant in the Au series, by fitting the data in Fig. 3(c) to $\lambda_{\mathrm{SD}}\tanh(t_{\mathrm{Au}}/2\lambda_{\mathrm{SD}})$,[33] we obtain λ_{SD} = 12.6 ± 2.5 nm for the Au films. The effective interfacial spin mixing conductance can be obtained from,[5,6,20,34,35]

$$g_{\uparrow\downarrow}^{eff} = \frac{4\pi M_{\mathrm{S}} t_{\mathrm{YIG}}}{g\mu_{\mathrm{B}}}(\alpha_{\mathrm{YIG/Au}} - \alpha_{\mathrm{YIG}}), \quad (2)$$

where M_s, g, and μ_B are the YIG saturation magnetization, Landé g factor, and Bohr magneton, respectively. To calculate $g_{\uparrow\downarrow}^{eff}$ we measure the spin pumping induced damping enhancement in YIG/Au bilayers ($\alpha_{\mathrm{YIG/Au}}$) as compared to a single YIG layer (α_{YIG}). Figure 2(c) shows that the damping constant is enhanced in Au/YIG bilayers as compared to a bare YIG film and the damping enhancement depends on the Au thickness. In order to accurately determine the damping constants, we performed frequency-dependent FMR measurements within the range of 2-20 GHz for a bare YIG(16 nm) film and six YIG(16 nm)/Au(t_{Au}) bilayers with t_{Au} = 5, 10, 20, 30, 50, and 100 nm, as shown in Fig. 4(a). They all exhibit a linear frequency dependence, and the Gilbert damping constant can be extracted from the slope by fitting the equation,[36]

$$\Delta H = \Delta H_{\mathrm{inh}} + \frac{4\pi\alpha f}{\sqrt{3}\gamma}, \quad (3)$$

where ΔH_{inh} is the inhomogeneous broadening [y-intercept in Fig. 4(a)] of YIG and $\gamma = 2\pi \times 28.0$ GHz/T (assuming g = 2). For the bare YIG film, we obtain a low damping constant of (6.13 ± 0.64) × 10^{-4}. When a 5 nm Au layer is deposited on YIG, the damping increases by 65% to (10.1 ± 0.5) × 10^{-4}. For thicker Au films, the damping constant continues to increase, as shown in

Table I and Fig. 4(b). The fact that the two samples with 50 and 100 nm Au exhibit almost the same damping constants indicates that the spin pumping induced damping enhancement has saturated by approximately 50 nm thickness of Au. From the measured damping constants, we calculate the Gilbert damping enhancement, $\alpha_{\mathrm{sp}} = \alpha_{\mathrm{YIG/Au}} - \alpha_{\mathrm{YIG}}$, for the six bilayer samples.

Using the damping constants and other experimentally measured parameters, we calculate the effective interfacial spin mixing conductances $g_{\uparrow\downarrow}^{eff}$ for all the samples as shown in Table I. The values of $g_{\uparrow\downarrow}^{eff}$ for the 50 and 100 nm Au samples are nearly identical and notably large, indicating a highly efficient interfacial spin transfer. We also note that the YIG/Au(5 nm) sample shows a smaller $g_{\uparrow\downarrow}^{eff}$ (by a factor of 6.6). From the obtained values of $g_{\uparrow\downarrow}^{eff}$, the spin current pumped from YIG into Au can be calculated by,[6,37]

$$J_{\mathrm{s}} = \frac{e}{2\pi} g_{\uparrow\downarrow} f P \left(\frac{\gamma h_{rf}}{4\pi f \alpha}\right)^2, \tag{4}$$

which is shown in Table I for the six samples. For the 5 nm Au sample, the injected spins propagate from the YIG/Au interface to the Au top surface without significant scattering. At the top surface, a portion of the spins are scattered by the surface while the rest are reflected back and accumulate in the Au layer. First, the scattering at the Au surface may provide additional surface-induced spin scattering to enhance the ISHE. Secondly, the spin accumulation in thin Au layers suppresses the angular momentum transfer at the YIG/Au interface, reducing the $g_{\uparrow\downarrow}^{eff}$ and J_s, which is similar to previous reports.[38,39] For the 50 and 100 nm Au samples, the film thicknesses are considerably larger than λ_{SD}; thus, most of the spins are scattered, producing an ISHE before reaching the Au top surface without much spin accumulation, resulting in large $g_{\uparrow\downarrow}$ and J_s.

Table I summarizes the spin pumping parameters of the YIG/Au(t_{Au}) bilayers. Using these

parameters, we calculated the spin Hall angles for the six Au films. From 20 to 100 nm Au thicknesses, the spin Hall angle varies between 0.016 and 0.020, which are essentially constant within the experimental uncertainty. This magnitude of θ_{SH} is reasonable for a heavy element with an atomic number of 79, and can be considered as the bulk value for Au. For thinner Au films, θ_{SH} doubles to 0.038 at 10 nm and more than doubles again to 0.087 for the 5 nm Au, which is similar to our previously reported value of 0.084.[18] Figure 4(b) shows that θ_{SH} and α_{sp} vary systematically as a function of the Au thickness with different effective length scales: θ_{SH} decreases quickly from 5 to 20 nm, then reaches essentially an equilibrium value from 20 to 100 nm; while α_{sp} continuously increases from 5 to 50 nm and has saturated by 50 nm. This behavior is similar to that observed in Co/Pt and Co/Cu/Pt systems with different lengthscales for damping and spin pumping.[40]

We speculate that the large value of the spin Hall angle for 5 nm Au is due to two factors. First, the resistivity of the 5 nm Au is about 3 times larger than the 50 and 100 nm Au, which can lead to a larger spin Hall angle, according the previous theoretical calculations.[16] However, this should not be the only reason for the large θ_{SH}. Specifically, for the 10 nm Au, its resistivity is comparable to those of the thicker Au films while the θ_{SH} of the 10 nm Au is twice as large. The second possible mechanism is that the Au top surface plays a significant role in spin scattering for the 5 and 10 nm films since their thicknesses are smaller than λ_{SD} (12.6 nm). The Au/air interface may contribute a Rashba-type spin-orbit coupling which enhances the ISHE in the thin Au layers. Previously, angle-resolved photoemission spectroscopy (ARPES) studies revealed a large surface spin-orbit splitting of about 110 meV on Au(111).[41,42] More recently, a spin pumping study of NiFe/Ag/Bi structures demonstrated very large Rashba coupling at the Ag/Bi interface and estimated an extraordinarily large spin Hall angle.[43] It has also been shown by

first-principles calculations and ARPES studies that Bi surfaces exhibit a strong Rashba spin-orbit splitting a few times larger than that on Au surfaces.[44] Thus, a considerable Rashba spin-orbit effect is expected to be present at the Au surface, which may enhance the ISHE in Au films thinner than the spin diffusion length. It should also be noted that Rashba spin-orbit coupling may exist at the YIG/Au interface, but we cannot probe it since all of the YIG/Au bilayers have the same YIG/Au interfaces and the same resulting Rashba contribution. The values of spin Hall angle obtained for the Au films reported here should be considered as effective spin Hall angles which represent the overall ability of a film of a given thickness to convert a spin current to a transverse charge current.

We point out that our fitting to extract λ_{SD} in Fig. 3(c) assumes θ_{SH} is independent of the Au thickness, while the obtained θ_{SH} varies for different thicknesses of Au layers, resulting in uncertainty in the determined λ_{SD}. However, this uncertainty in λ_{SD} does not affect the main result of this work, i.e., the enhancement of θ_{SH} in the 5 and 10 nm Au. To demonstrate this point, Table II shows the values of θ_{SH} for the 5, 10, 20, 30, 50 and 100 nm Au layers as λ_{SD} is varied from 12.6 nm to 10, 20, 30, and 60 nm.[45] Clearly, the values of θ_{SH} for the 5 and 10 nm Au films are essentially unchanged for λ_{SD} between 10 and 60 nm, and are therefore reliable. As the Au thickness increases, the variation in θ_{SH} gradually becomes larger. For the 100 nm Au sample, θ_{SH} changes between 0.0052 and 0.021 within the range of λ_{SD}. We also note that in Fig. 3(c), the value of V_{ISHE}/Rw (ISHE-induced charge current per unit width) is essentially unchanged for $t_{Au} \geq 30$ nm, indicating that λ_{SD} should be smaller than 30 nm. Thus, despite the uncertainty in λ_{SD}, we are confident that θ_{SH} is enhanced for the 5 nm Au layer ($\theta_{SH} = 0.087$) as compared to thicker Au layers that exhibit bulk-like values of the spin Hall angle.

In conclusion, we studied the thickness dependence of the spin Hall angle of Au layers using FMR spin pumping in YIG/Au bilayers by quantitative measurements of the ISHE voltage, Gilbert damping enhancement, spin diffusion length, interfacial spin mixing conductance, and spin current. We find that the spin Hall angle is significantly enhanced for films thinner than the spin diffusion length.

Acknowledgements

This work was primarily supported by National Science Foundation under Grant No. DMR-1507274 (sample growth and characterization, ISHE measurements and analysis). This work was supported in part by US Department of Energy (DOE), Office of Science, Basic Energy Sciences, under Award No. DE-FG02–03ER46054 (FMR measurements and modeling) and the Center for Emergent Materials, an NSF-funded MRSEC, under Grant No. DMR-1420451 (STEM characterization).

References:

1. Y. Kajiwara, K. Harii, S. Takahashi, J. Ohe, K. Uchida, M. Mizuguchi, H. Umezawa, H. Kawai, K. Ando, K. Takanashi, S. Maekawa, and E. Saitoh, *Nature* **464**, 262 (2010).
2. K. Uchida, S. Takahashi, K. Harii, J. Ieda, W. Koshibae, K. Ando, S. Maekawa, and E. Saitoh, *Nature* **455**, 778 (2008).
3. E. Saitoh, M. Ueda, H. Miyajima, and G. Tatara, *Appl. Phys. Lett.* **88**, 182509 (2006).
4. M. V. Costache, M. Sladkov, S. M. Watts, C. H. van der Wal, and B. J. van Wees, *Phys. Rev. Lett.* **97**, 216603 (2006).
5. O. Mosendz, V. Vlaminck, J. E. Pearson, F. Y. Fradin, G. E. W. Bauer, S. D. Bader, and A. Hoffmann, *Phys. Rev. B* **82**, 214403 (2010).
6. E. Shikoh, K. Ando, K. Kubo, E. Saitoh, T. Shinjo, and M. Shiraishi, *Phys. Rev. Lett.* **110**, 127201 (2013).
7. T. Kimura and Y. Otani, *Phys. Rev. Lett.* **99**, 196604 (2007).
8. M. Farle, *Rep. Prog. Phys.* **61**, 755 (1998).
9. K. Uchida, J. Xiao, H. Adachi, J. Ohe, S. Takahashi, J. Ieda, T. Ota, Y. Kajiwara, H. Umezawa, H. Kawai, G. E. W. Bauer, S. Maekawa, and E. Saitoh, *Nat. Mater.* **9**, 894 (2010).
10. I. Zutic, J. Fabian, and S. Das Sarma, *Rev. Mod. Phys.* **76**, 323 (2004).
11. A. Azevedo, L. H. V. Leao, R. L. Rodriguez-Suarez, A. B. Oliveira, and S. M. Rezende, *J. Appl. Phys.* **97**, 10C715 (2005).
12. S. O. Valenzuela and M. Tinkham, *Nature* **442**, 176 (2006).
13. K. Ando, S. Takahashi, J. Ieda, H. Kurebayashi, T. Trypiniotis, C. H. W. Barnes, S. Maekawa, and E. Saitoh, *Nat. Mater.* **10**, 655 (2011).
14. O. Mosendz, J. E. Pearson, F. Y. Fradin, G. E. W. Bauer, S. D. Bader, and A. Hoffmann, *Phys. Rev. Lett.* **104**, 046601 (2010).
15. A. Hoffmann, *IEEE Trans. Magn.* **49**, 5172 (2013).
16. T. Tanaka, H. Kontani, M. Naito, T. Naito, D. S. Hirashima, K. Yamada, and J. Inoue, *Phys. Rev. B* **77**, 165117 (2008).
17. M. Morota, Y. Niimi, K. Ohnishi, D. H. Wei, T. Tanaka, H. Kontani, T. Kimura, and Y. Otani, *Phys. Rev. B* **83**, 174405 (2011).
18. H. L. Wang, C. H. Du, Y. Pu, R. Adur, P. C. Hammel, and F. Y. Yang, *Phys. Rev. Lett.* **112**, 197201 (2014).
19. D. D. Sarma, *Proc. Indian Acad. Sci.* **90**, 19 (1981).
20. B. Heinrich, C. Burrowes, E. Montoya, B. Kardasz, E. Girt, Y.-Y. Song, Y. Y. Sun, and M. Z. Wu, *Phys. Rev. Lett.* **107**, 066604 (2011).
21. C. Burrowes, B. Heinrich, B. Kardasz, E. A. Montoya, E. Girt, Y. Sun, Y. Y. Song, and M. Z. Wu, *Appl. Phys. Lett.* **100**, 092403 (2012).
22. M. Isasa, E. Villamor, L. E. Hueso, M. Gradhand, and F. Casanova, *Phys. Rev. B* **91**, 024402 (2015).

23. T. Seki, I. Sugai, Y. Hasegawa, S. Mitani, and K. Takanashi, *Solid State Comm.* **150**, 496 (2010).
24. D. Qu, S. Y. Huang, J. Hu, R. Q. Wu, and C. L. Chien, *Phys. Rev. Lett.* **110**, 067206 (2013).
25. V. Vlaminck, J. E. Pearson, S. D. Bader, and A. Hoffmann, *Phys. Rev. B* **88**, 064414 (2013).
26. T. Seki, Y. Hasegawa, S. Mitani, S. Takahashi, H. Imamura, S. Maekawa, J. Nitta, and K. Takanashi, *Nat. Mater.* **7**, 125 (2008).
27. H. Y. Hung, G. Y. Luo, Y. C. Chiu, P. Chang, W. C. Lee, J. G. Lin, S. F. Lee, M. Hong, and J. Kwo, *J. Appl. Phys.* **113**, 17C507 (2013).
28. G. Mihajlović, J. E. Pearson, M. A. Garcia, S. D. Bader, and A. Hoffmann, *Phys. Rev. Lett.* **103**, 166601 (2009).
29. A. J. Hauser, J. M. Lucy, H. L. Wang, J. R. Soliz, A. Holcomb, P. Morris, P. M. Woodward, and F. Y. Yang, *Appl. Phys. Lett.* **102**, 032403 (2013).
30. C. H. Du, R. Adur, H. L. Wang, A. J. Hauser, F. Y. Yang, and P. C. Hammel, *Phys. Rev. Lett.* **110**, 147204 (2013).
31. H. L. Wang, C. H. Du, Y. Pu, R. Adur, P. C. Hammel, and F. Y. Yang, *Phys. Rev. B.* **88**, 100406(R) (2013).
32. F. D. Czeschka, L. Dreher, M. S. Brandt, M. Weiler, M. Althammer, I. M. Imort, G. Reiss, A. Thomas, W. Schoch, W. Limmer, H. Huebl, R. Gross, and S. T. B. Goennenwein, *Phys. Rev. Lett.* **107**, 046601 (2011).
33. H. Nakayama, K. Ando, K. Harii, T. Yoshino, R. Takahashi, Y. Kajiwara, K. Uchida, Y. Fujikawa, and E. Saitoh, *Phys. Rev. B* **85**, 144408 (2012).
34. Y. Tserkovnyak, A. Brataas, and G. E. W. Bauer, *Phys. Rev. B* **66**, 224403 (2002).
35. C. T. Boone, H. T. Nembach, J. M. Shaw, and T. J. Silva, *J. Appl. Phys.* **113**, 153906 (2013).
36. S. S. Kalarickal, P. Krivosik, M. Wu, C. E. Patton, M. L. Schneider, P. Kabos, T. J. Silva, and J. P. Nibarger, *J. Appl. Phys.* **99**, 093909 (2006).
37. K. Ando, S. Takahashi, J. Ieda, Y. Kajiwara, H. Nakayama, T. Yoshino, K. Harii, Y. Fujikawa, M. Matsuo, S. Maekawa, and E. Saitoh, *J. Appl. Phys.* **109**, 103913 (2011).
38. C. H. Du, H. L. Wang, F. Y. Yang, and P. C. Hammel, *Phys. Rev. Applied* **1**, 044004 (2014).
39. M. H. Nguyen, D. C. Ralph, and R. A. Buhrman, *Phys. Rev. Lett.* **116**, 126601 (2016).
40. J. C. Rojas-Sanchez, N. Reyren, P. Laczkowski, W. Savero, J. P. Attane, C. Deranlot, M. Jamet, J. M. George, L. Vila, and H. Jaffres, *Phys. Rev. Lett.* **112**, 106602 (2014).
41. S. LaShell, B. A. McDougall, and E. Jensen, *Phys. Rev. Lett.* **77**, 3419 (1996).
42. G. Nicolay, F. Reinert, S. Hufner, and P. Blaha, *Phys. Rev. B* **65**, 033407 (2002).
43. J. C. Rojas Sanchez, L. Vila, G. Desfonds, S. Gambarelli, J. P. Attane, J. M. De Teresa, C. Magen, and A. Fert, *Nature Comm.* **4**, 2944 (2013).

44. Y. M. Koroteev, G. Bihlmayer, J. E. Gayone, E. V. Chulkov, S. Blugel, P. M. Echenique, and P. Hofmann, *Phys. Rev. Lett.* **93**, 046403 (2004).
45. T. Kimura, J. Hamrle, and Y. Otani, *Phys. Rev. B* **72**, 014461 (2005).

Figure Captions:

Figure 1: (a) Semi-log 2θ-ω XRD scan of a 16 nm YIG film grown on GGG(111) around the YIG(444) peak, showing Laue oscillations and an arrow indicating the position of the YIG(444) peak. (b) XRR scan (red) of a YIG(16 nm)/Au(41 nm) bilayer. The simulation (blue) gives an interfacial roughness of less than 1 Å. (c) STEM image of the YIG/GGG(111) interface shows complete epitaxy, clear Y/Fe atomic ordering, and no detectable structural defects throughout the films.

Figure 2: (a) Schematic of inverse spin Hall measurement setup. (b) ISHE voltage measurement for the 5, 30, 50, and 100 nm Au layers on YIG(16 nm) taken at P_{rf} = 200 mW. (c) Derivative FMR absorption spectra for a bare YIG(16 nm) film, as well as YIG/Au(5 nm), YIG/Au(30 nm), and YIG/Au(50 nm) bilayers.

Figure 3. Au thickness dependencies of (a) ISHE voltage, (b) resistivity (ρ), and (c) normalized ISHE charge current, V_{ISHE}/Rw, of the YIG/Au(t_{Au}) bilayers, where R and w are the resistance and sample width of each bilayer. The blue curve in (c) is a fitting to extract the spin diffusion length.

Figure. 4. (a) Frequency dependencies of the FMR linewidth from 2 to 20 GHz for a YIG(16 nm) bare film, and six YIG/Au(t_{Au}) bilayers with t_{Au} = 5, 10, 20, 30, 50, and 100 nm. The straight lines are linear least-squares fits to the data, yielding Gilbert damping constant of 6.13×10^{-4}, 10.1×10^{-4}, 23.4×10^{-4}, 27.3×10^{-4}, 30.4×10^{-4}, 33.8×10^{-4}, and 34.1×10^{-4}, respectively. (b) Au thickness dependencies of spin Hall angle (red) and spin pumping induced damping enhancement (blue).

Table I. Parameters of different Au thicknesses on YIG(16 nm), including: ISHE voltages, resistivities, and Gilbert damping enhancements from the measurements, as well as calculated values of interfacial spin mixing conductances, spin Hall angles, and spin currents.

t_{Au} (nm)	V_{ISHE} (μV)	$\alpha_{YIG/Au}$ (10^{-4})	α_{YIG} (10^{-4})	$\alpha_{sp} = \alpha_{YIG/Au} - \alpha_{YIG}$ (10^{-4})	ρ (μΩ-cm)	$g_{\uparrow\downarrow}$ (10^{18} m^{-2})	θ_{SH} (10^{-2})	J_s (10^6 A/m^2)
5	143	10.1±0.5	6.13±0.64	3.97±0.81	30.6	0.69±0.14	8.7±2.5	0.75±0.22
10	131	23.4±0.5	7.80±0.80	15.6±0.9	13.7	2.7±0.2	3.8±0.8	1.81±0.39
20	64.1	27.3±0.7	7.80±0.80	19.5±1.1	14.0	3.4±0.2	1.8±0.4	2.27±0.48
30	60.5	30.4±1.1	7.80±0.80	22.6±1.4	11.4	3.9±0.2	2.0±0.5	2.63±0.56
50	27.5	33.8±0.7	7.80±0.80	26.0±1.1	11.9	4.5±0.3	1.6±0.4	3.02±0.47
100	14.2	34.1±1.1	7.80±0.80	26.3±1.4	8.8	4.6±0.3	1.7±0.5	3.06±0.41

Table II. A comparison of spin Hall angles calculated for the Au films as the spin diffusion length is varied. The first row shows θ_{SH} for the experimentally obtained λ_{SD} = 12.6 nm (bold). The next four rows show θ_{SH} for hypothetical values of λ_{SD} ranging from 10 to 60 nm to demonstrate how θ_{SH} is affected by λ_{SD}.

λ_{SD} (nm)	θ_{SH}					
	5 nm	10 nm	20 nm	30 nm	50 nm	100 nm
12.6	**0.087**	**0.038**	**0.18**	**0.020**	**0.016**	**0.017**
10	0.087	0.039	0.020	0.024	0.019	0.021
20	0.086	0.037	0.016	0.016	0.011	0.011
30	0.086	0.036	0.015	0.015	0.0093	0.0076
60	0.085	0.036	0.015	0.014	0.0080	0.0052

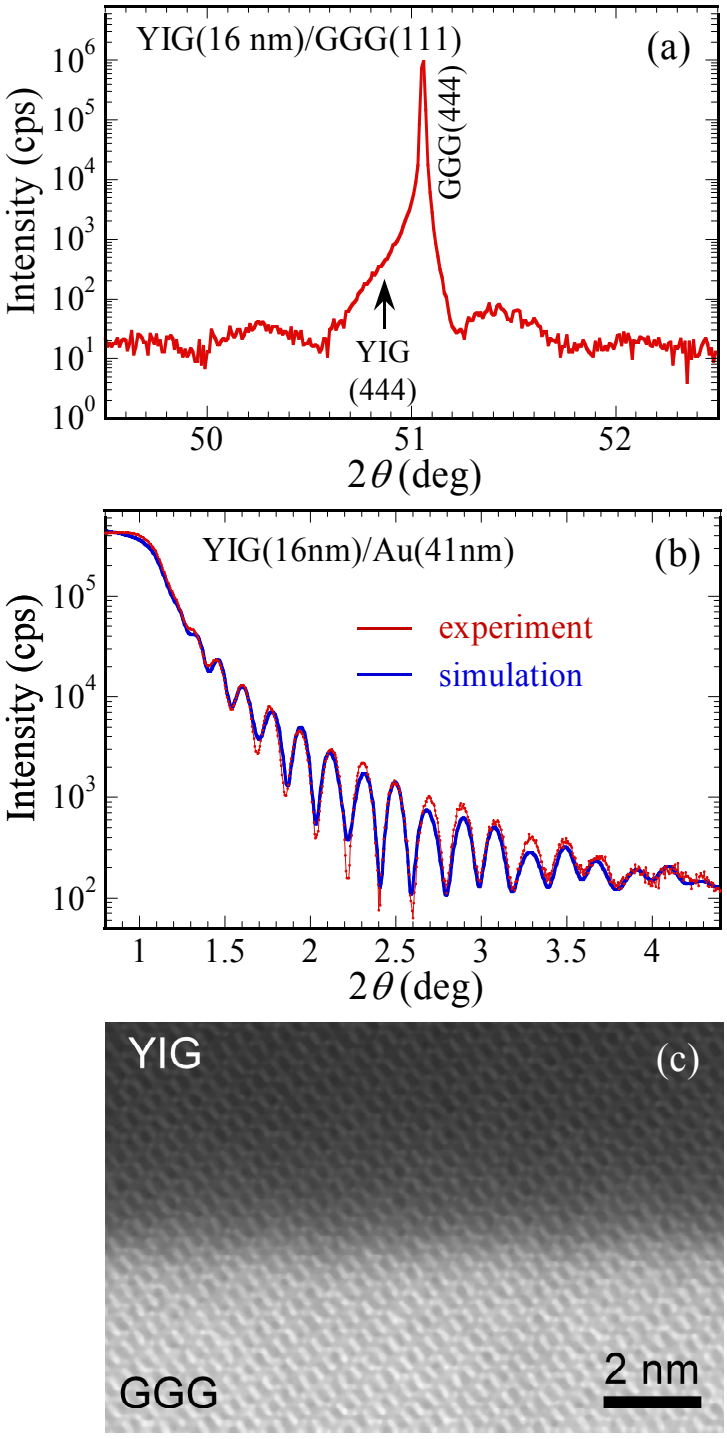
YIG(16 nm)/GGG(111)
(a)
GGG(444)
YIG
(444)
Intensity (cps)
2θ (deg)
YIG(16nm)/Au(41nm)
(b)
experiment
simulation
Intensity (cps)
2θ (deg)
YIG
(c)
GGG
2 nm

Figure 1.

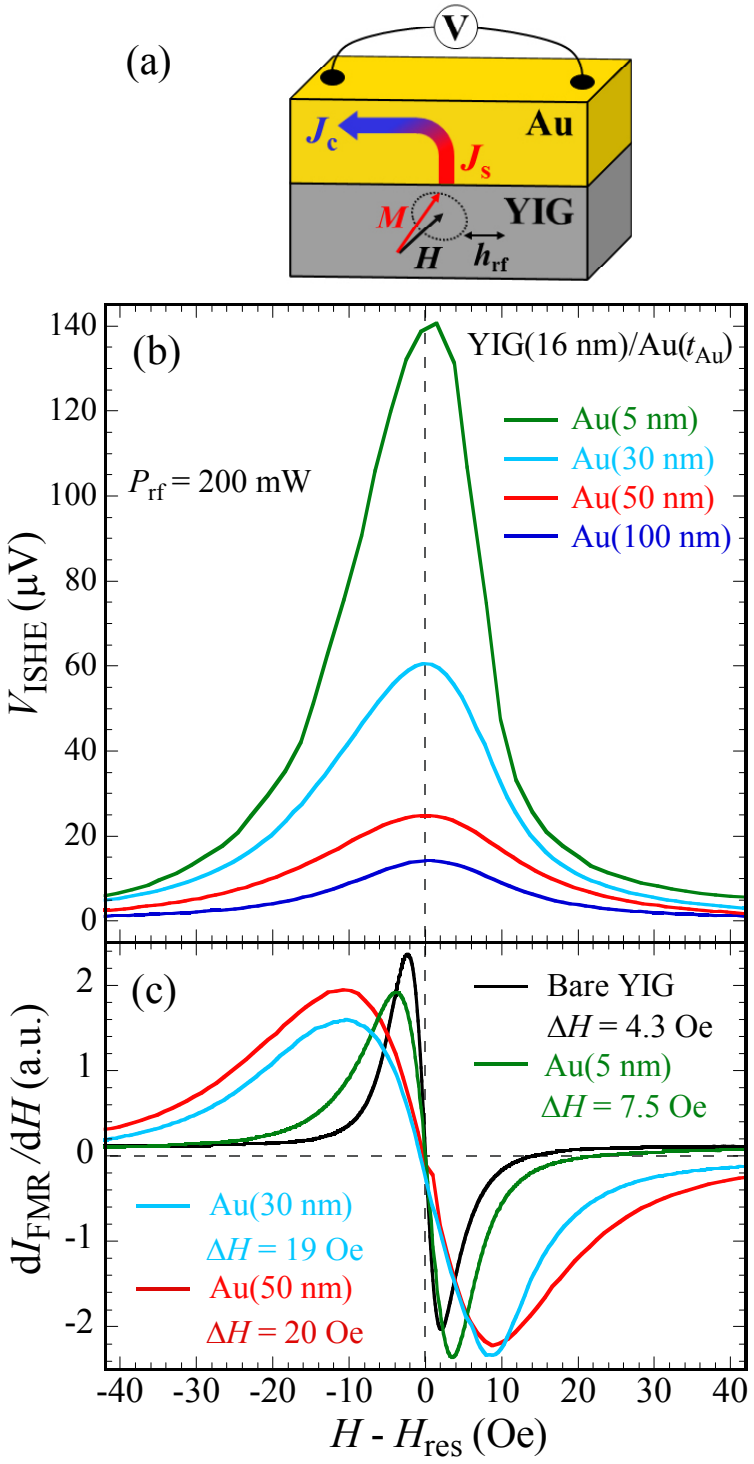
(a)
V
Au
J_c
J_s
YIG
M
H
h_{rf}
(b)
YIG(16 nm)/Au(t_{Au})
Au(5 nm)
Au(30 nm)
Au(50 nm)
Au(100 nm)
P_{rf} = 200 mW
V_{ISHE} (μV)
(c)
Bare YIG
ΔH = 4.3 Oe
Au(5 nm)
ΔH = 7.5 Oe
Au(30 nm)
ΔH = 19 Oe
Au(50 nm)
ΔH = 20 Oe
dI_{FMR}/dH (a.u.)
H - H_{res} (Oe)

Figure 2.

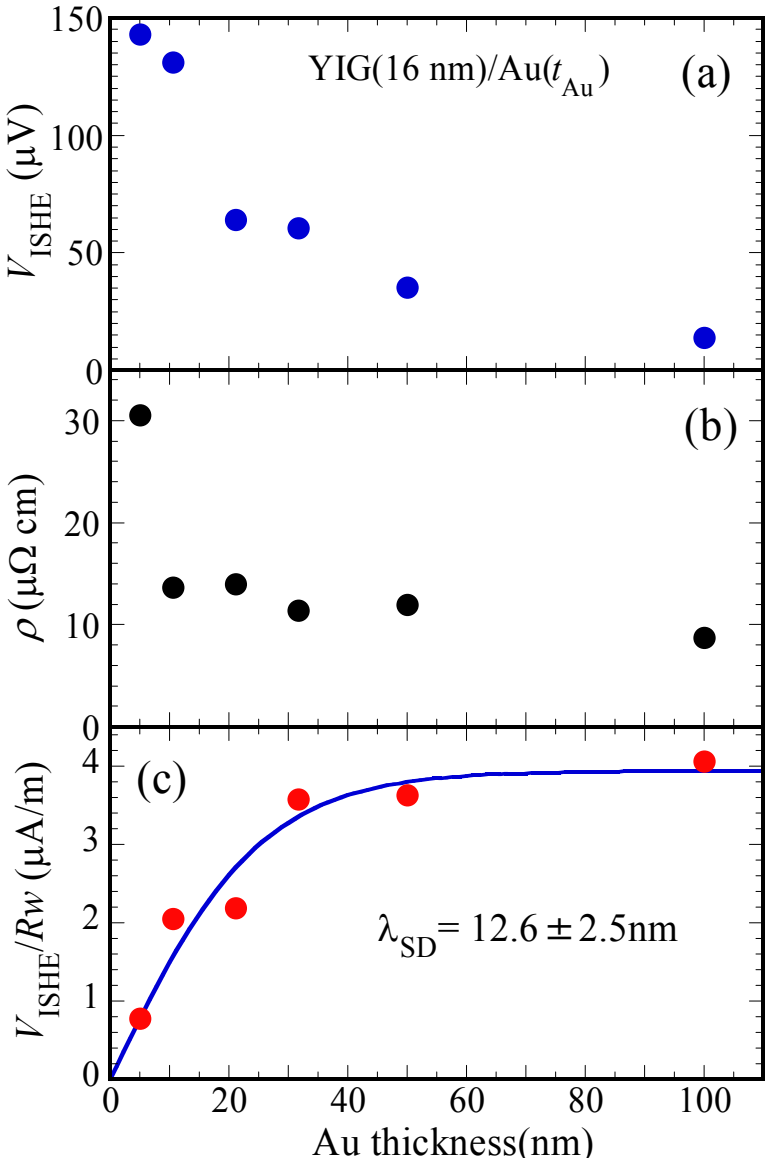
YIG(16 nm)/Au(t_{Au})
(a)
V_{ISHE} (μV)
150
100
50
0
(b)
ρ (μΩ cm)
30
20
10
0
(c)
V_{ISHE}/Rw (μA/m)
4
3
2
1
0
λ_{SD}= 12.6 ± 2.5nm
0
20
40
60
80
100
Au thickness(nm)

Figure. 3.

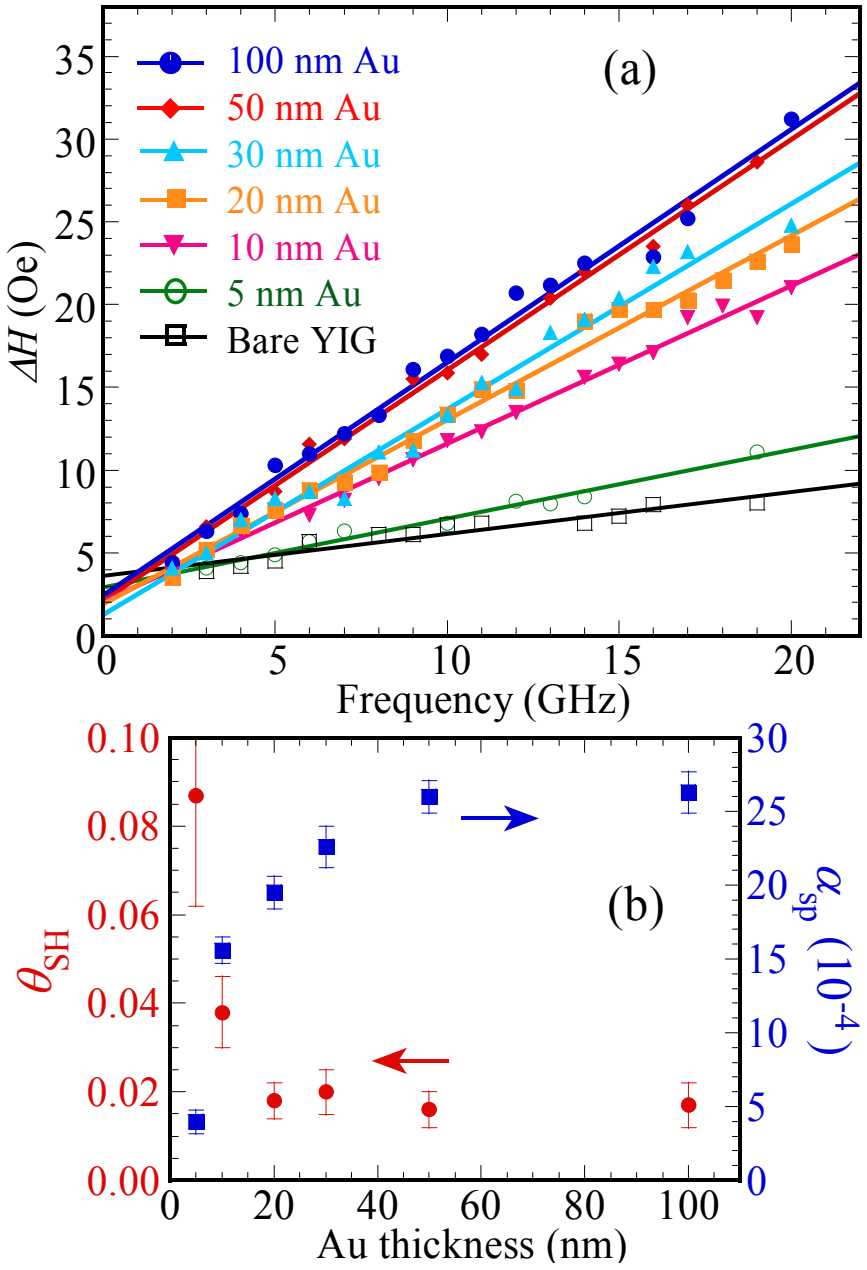
100 nm Au
50 nm Au
30 nm Au
20 nm Au
10 nm Au
5 nm Au
Bare YIG
(a)
ΔH (Oe)
Frequency (GHz)
(b)
θSH
αsp (10-4)
Au thickness (nm)

Figure 4.